Progress in Nuclear Energy 168 (2024) 105028

Contents lists available at ScienceDirect

Progress in Nuclear Energy

journal homepage: www.elsevier.com/locate/pnucene

Numerical study on flow structure and heat transfer of supercritical CO_2 in tubes with different inclination angles

Junren Hou [a,b], Yuan Zhou [b,*], Yuan Yuan [b], Shanfang Huang [a]

[a] Department of Engineering Physics, Tsinghua University, Beijing, 100084, China
[b] College of Physics, Sichuan University, Chengdu, 610065, China

ARTICLE INFO

Keywords:
Supercritical CO_2
Inclined tubes
Turbulent Prandtl number
Flow structure
Heat transfer

ABSTRACT

To reveal how buoyancy affects heat transfer of supercritical carbon dioxide (sCO_2), the flow and heat transfer characteristics of sCO_2 in circular tubes with an inner diameter of 19 mm at different inclination angles were numerically investigated. The calculation results of RNG $k-\epsilon$, RKE $k-\epsilon$, SST $k-\omega$ and SST $k-\omega$ using a variable turbulent Prandtl number model (TWL model) have been compared with experimental data. The TWL model is chosen for numerical calculations because of its significant advantage in predicting wall temperature. Both forced convection (Richardson number $Ri < 0.1$, weak buoyancy) and mixed convection ($Ri > 0.1$, strong buoyancy) of sCO_2 are calculated. Result shows that the position of the velocity peak moves upward, then downward as the flow changes from vertical upward (inclination angle $\alpha = 0°$) to horizontal flow ($\alpha = 90°$) due to the secondary flow caused by radial buoyancy and the increase in velocity magnitude in the near top wall region caused by axial buoyancy. Under strong buoyancy effects, as α increases from 0° to 90°, the heat transfer deterioration (HTD) becomes severe when $\alpha < 15°$, then alleviated and finally severe again when α approaches 90° due to the change of the heat transfer mechanism. This work deepens our understanding of sCO_2 heat transfer and may provide reference for the design of heat exchangers in nuclear reactors.

1. Introduction

Carbon dioxide (CO_2) possesses favorable characteristics such as non-toxicity, non-flammability, chemical stability, widespread availability, and cost-effectiveness, rendering it a suitable candidate for implementation as a working fluid in supercritical CO2 (sCO_2) Brayton cycles. These cycles have several advantages over conventional power cycles, such as reduced compression work due to the incompressible behavior of CO_2 near the critical point (7.38 MPa, 31 °C) (Ahn et al., 2015; Dostal et al., 2004) and smaller size of turbomachinery and heat exchangers owing to the high density of sCO2 throughout the cycle. Therefore, sCO_2 and the relevant cycles have been widely applied to various energy sources, such as nuclear power(Wu et al., 2020), solar energy(Wang and He, 2017), and high-temperature fuel cells(Sánchez et al., 2011).

One of the distinctive features of sCO_2 is the rapid variation of its thermophysical properties near the pseudocritical temperature (T_{pc}), as shown in Fig. 1. The specific heat and thermal conductivity exhibit peaks, while the density and viscosity decrease sharply in this region. This phenomenon leads to complex and unique flow and heat transfer characteristics of sCO_2, which have attracted considerable attention from researchers.

Most prior investigations regarding sCO_2 heat transfer have predominantly centered around vertical flow, which is relevant to nuclear reactors using the sCO_2 indirect cycle, transpiration cooling of high heat flux surfaces. Kim et al. (Kim and Kim, 2011) performed experiments to investigate the turbulent heat transfer of sCO_2 in vertical upward and downward flow. They observed a wall temperature peak for upward flow and none for downward flow at moderate wall heat flux and low mass flux conditions. Bae et al. (2010) conducted experimental tests to investigate the heat transfer of sCO_2 in vertical upward and downward flow in a circular tube with a diameter of 6.32 mm. They observed a significant decrease in Nusselt number in the range of $10^{-6} < Gr_b/Re_b^{2.7} < 2 \times 10^{-5}$ (where Gr_b and Re_b denote the Grashoff number and Reynolds number determined by the bulk temperature) before entering a serious heat transfer deterioration regime.

In view of the heat transfer deterioration (HTD), many scholars have tried to analyze the intrinsic mechanism in detail. Buzzi et al. (2019) tried to provide a description of the reasons for its occurrence with numerical simulation. The simulation results of wall temperature

* Corresponding author.
E-mail address: zhouyuan1911@126.com (Y. Zhou).

https://doi.org/10.1016/j.pnucene.2023.105028
Received 4 July 2023; Received in revised form 8 December 2023; Accepted 13 December 2023
Available online 18 December 2023

Nomenclature

Latin symbols

A	constant of TWL model
Bo^*	buoyancy factor
C_p	specific heat at constant pressure, J/(kg·K)
d	inner diameter of tube, m
g	gravitational acceleration, m/s^2
G	mass flux, kg/(m^2·s)
Gr	Grashof number
Gr^*	Grashof number based on heat flux
$\overline{Gr}$	Grashof number based on mean density
H	enthalpy, J/kg
h	heat transfer coefficient, W/(m^2·K)
l	effective heating length, m
m	mass flow rate, kg/s
n_1, n_2, n_3	number of the edge node
$Power$	heating power, W
Pr	Prandtl number
Pr_t	turbulent Prandtl number
q	inner wall heat flux, W/m^2
r	radial coordinate, m
R	tube radius, m
Re	Reynolds number
Ri	Richardson number
T	temperature, °C
TKE, k	turbulence kinetic energy, m^2/s^2
u	component of the velocity vector, m/s
v	velocity magnitude, m/s
x, y, z	coordinates
y^+	non-dimensional distance from wall

Greek symbols

α	inclination angle of tube
θ	circumferential angle of tube
λ	thermal conductivity, W/(m·K)
μ	molecular viscosity, kg/(m·s)
μ_e	effective viscosity, kg/(m·s)
μ_t	turbulent viscosity, kg/(m·s)
ρ	density, kg/m^3
$\overline{\rho}$	Integrated density, kg/m^3

Subscripts

b	bulk temperature
f	fluid temperature
i	general spatial indices
in	inlet
out	outlet
pc	pseudo-critical
w	inside wall

Abbreviation

AKN	Abe, Kondoh and Nagano turbulence model(Abe et al., 1994)
HTD	heat transfer deterioration
sCO_2	supercritical carbon dioxide
RANS	Reynolds-Averaged Navier-Stokes

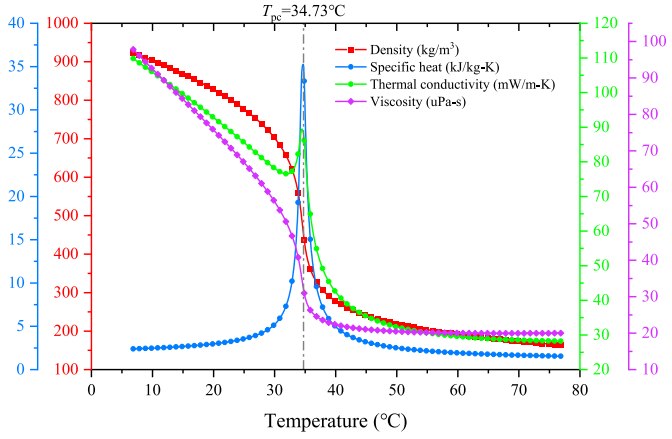

Fig. 1. Thermophysical properties of sCO_2 at 8.0 MPa (Lemmon et al., 2002).

correspond well with the experimental results. Cheng et al. (2017) numerically analyzed the two wall temperature peaks in circular tubes at high heat fluxes and low mass fluxes. The findings indicate that the initial peak is attributed to the buoyancy effect, while the subsequent peak arises from the shear stress-induced flattening of the velocity distribution in the main flow region. This flattening, in turn, results in a reduction of turbulent kinetic energy, further compromising heat transfer and giving rise to the second peak.

Recently, more attention has been paid to the applications of sCO_2 in horizontal operating conditions, such as printed circuit heat exchangers and air cooling sCO_2 heat exchangers. Zhang et al. (2019) numerically investigated the coupled heat transfer characteristics of sCO_2 in horizontal semicircular channels using SST k-ω model. The numerical results show that the buoyancy effect becomes weaker with increasing mass flow rate, and that the asymmetric flow has better heat transfer performance than the symmetric flow at low mass flow rate. Wang et al., 2018a, 2018b numerically studied the flow and heat transfer characteristics of turbulent sCO_2 in a large horizontal tube under heating and cooling conditions using AKN k-ε model (which is proposed by Abe, Kondoh and Nagano(Abe et al., 1994)). The findings indicate that buoyancy effects predominantly impact the flow structure and turbulence levels by means of the induced secondary circulation. Particularly under heating conditions, stronger buoyancy effects are observed at higher heat flux values, leading to a greater temperature disparity between the upper and lower surfaces of the tube. Under cooling conditions, as the values of Richardson number (Ri) continue increasing within $Ri > 0.1$, the buoyant force is enhanced, which in turn deteriorates the heat transfer near pseudo-critical temperature (T_{pc}).

With the development of sCO_2 applications, the flow and heat transfer of sCO_2 in inclined circular tubes have also received great attention from many researchers(Wang et al., 2022). Forooghi and Hooman (2013) numerically studied the convection heat transfer in inclined pipes with significant buoyancy influence using the V2F model. They found that the heat transfer deterioration due to reduced turbulence production in vertical upward flow also occurs in inclined circular tubes, and it becomes less pronounced when $\alpha > 30°$. Yang et al. (2013) numerically simulated the laminar mixed convective flow and heat transfer of sCO_2 in an inclined tube with a diameter of 0.5 mm under cooling condition with a constant wall temperature. The result shows that the horizontal flow has the highest heat transfer coefficient among the selected inclination angles. The inclined flows at $\alpha = 60°$ and 120° also have better heat transfer performance than other angles. Dong et al. (2022) investigated the flow and heat transfer of sCO_2 in tubes with inclination angle $\alpha = 60°$. They observed two wall temperature peaks in the circumferential direction of the tube when the inlet temperature was relatively low. Diao et al. (2019) conducted a numerical simulation on the turbulent mixed convection and heat exchange of sCO_2 cooled by constant heat flux in an inclined circular channel. They found that the

maximum heat transfer coefficient (HTC) decreases significantly with the deviation of the operating pressure from the critical pressure. A nonlinear stability analysis on sCO_2 in an inclined heating tube is also conducted by Singh (Singh and Singh, 2019). Based on the existing literature, it appears that most studies have focused on analyzing the heat transfer characteristics at a limited range of angles, such as 30°, 60°, and 90°. However, to date, comprehensive investigations into the overall trends of heat transfer and flow characteristics across the entire angular range from 0° to 180° have yet to be conducted.

As discussed above, Computational Fluid Dynamics (CFD) method is a popular tool to investigate the heat transfer mechanism(He et al., 2021; Li et al., 2020; Qin et al., 2019; Sun et al., 2022). Among various CFD methods, Reynolds-Averaged Navier-Stokes (RANS) method is the most widely adopted one for turbulent sCO_2 heat transfer simulations. This is because it can offer valuable and reliable insights into the thermal-hydraulics of turbulent sCO_2 flows with reasonable accuracy and low computational cost(Chen et al., 2018; Yang et al., 2010; Yu et al., 2018). To improve the prediction accuracy of the RANS model, some modifications have been proposed for the turbulence model. In 2016, a variable turbulent Prandtl number (Pr_t) model (TWL) is proposed by Tang(Tang et al., 2016). The comparison between TWL model and 14 experimental data shows that TWL model can correctly predict the heat transfer deterioration (HTD) of supercritical fluid. Guo et al. (2019) studied the thermal-hydraulic characteristics of sCO_2 in vertical tubes under cooling and heating conditions with TWL model. Du et al. (2020) added pressure and tube diameter correction factors to the model considering the effects of pressure and tube diameter. The modified variable Pr_t model was validated by comparing it with 26 reported experimental data, especially for HTD cases. In Section 3.2, the TWL model is compared with other turbulence models. The TWL model has obvious advantages in predicting heat transfer deterioration. Therefore, the TWL model is chosen for simulation calculation in this paper.

Despite considerable research efforts, the intricate heat transfer mechanism of sCO_2 heat transfer remains inadequately understood. In this numerical study, the authors examined the flow structure and heat transfer characteristics of sCO_2 in circular tubes inclined at various angles using the TWL model. The primary goal is to gain insights into the progressive influence of buoyancy on heat transfer and flow as the inclination angle α changes from 0° to 180°, which is still a fundamental question yet to be resolved. Additionally, the authors investigated the impact of buoyancy on heat transfer deterioration at small inclination angles, which is a crucial consideration for optimizing heat exchanger design (Forooghi and Hooman, 2013). Findings from this study could significantly advance our understanding of sCO_2 heat transfer and serve as a reference for the design of advanced heat exchangers in nuclear reactors.

The structure of this paper is as follows: firstly, a numerical model based on TWL model is established and its mesh independence is verified in detail. Then, the influence of buoyancy on sCO_2 flow structure and its internal mechanism are discussed in detail. Finally, the influence and mechanism of α on sCO_2 heat transfer under strong/weak buoyancy are analyzed.

2. Numerical approach

2.1. Governing equations

Governing equations for steady flow simulated in this study are given by (Wang et al., 2019):

Continuity:

$$\frac{\partial}{\partial x_i}(\rho u_i) = 0 \tag{1}$$

Momentum:

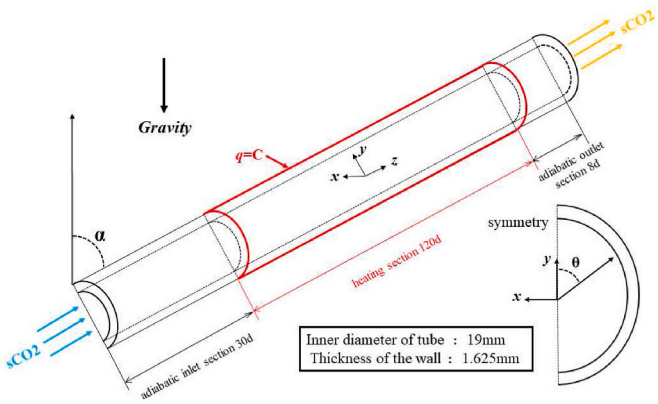

Fig. 2. Physical model and boundary conditions of the inclined tube.

$$\frac{\partial}{\partial x_i}(\rho u_i u_j) = \rho g_j - \frac{\partial}{\partial x_j}\left(P + \frac{2}{3}\mu_e \frac{\partial u_i}{\partial x_i}\right) + \frac{\partial}{\partial x_i}\left[\mu_e\left(\frac{\partial u_i}{\partial x_j} + \frac{\partial u_j}{\partial x_i}\right)\right] \tag{2}$$

Energy :

$$\frac{\partial}{\partial x_i}(\rho u_i H) = \frac{\partial}{\partial x_i}\left[\left(\lambda + \frac{C_p \mu_t}{Pr_t}\right)\frac{\partial T}{\partial x_i}\right] \tag{3}$$

where μ_e is the effective viscosity defined as the sum of the molecular viscosity μ and the turbulent viscosity μ_t defined as Eq. (6) in SST k-ω model. In the SST k-ω turbulence model, the transport equations of turbulent kinetic energy k and specific dissipation rate ω are defined in Eq. (4) and (5). λ indicates the thermal conductivity and Pr_t is the turbulence Prandtl number which is defined as Eq. (7) in TWL model (A is recommended to be 15 (Tang et al., 2016)).

$$\frac{\partial}{\partial x_i}(\rho k u_i) = \frac{\partial}{\partial x_i}\left(\Gamma_k \frac{\partial k}{\partial x_j}\right) + G_k - Y_k + S_k \tag{4}$$

$$\frac{\partial}{\partial x_j}(\rho \omega u_j) = \frac{\partial}{\partial x_j}\left(\Gamma_\omega \frac{\partial \omega}{\partial x_j}\right) + G_\omega - Y_\omega + D_\omega + S_\omega \tag{5}$$

$$\mu_t = \alpha^* \frac{\rho k}{\omega} \tag{6}$$

$$Pr_t = \begin{cases} 1.0 & \frac{\mu_t}{\mu} < 0.2 \\ 0.85 + \frac{Pr}{A} & 0.2 \leqslant \frac{\mu_t}{\mu} \leqslant 10 \\ 0.85 & 10 < \frac{\mu_t}{\mu} \end{cases} \tag{7}$$

where α^* is the damping coefficient of the turbulent viscosity causing a low-Reynolds number correction (see Ref. (Fluent, 2011)). The Pr in Eq. (7) refers to the Prandtl number of the fluid here, which is determined by the physical properties of sCO_2. Under the working conditions calculated in the paper, the value of Pr varies between 1 and 35. The computational fluid dynamics (CFD) software employed in this study is ANSYS FLUENT 2021R1, a commercially available software that utilizes the finite volume method for discretizing the governing equations.

2.2. Physical model and boundary conditions

The RANS models are validated by experimental data from Weinberg (Weinberg, 1972) and a similar physical model is used to analyze the flow structure and heat transfer of sCO_2 in this study. Due to the symmetry of the physical phenomenon on both sides, only half of the tube is considered to reduce the computational cost. As shown in Fig. 2, the circular tube has an inner diameter of 19 mm, a wall thickness of 1.625

Table 1
Thermal physical properties of solid(Sweet et al., 1987).

$T(^{\circ}C)$	ρ(kg /m^3)	λ(W /(m ·K))	c_p(J /kg ·K)
0	7930	14.5	460.5
20.75		14.8	472.9
26.55		15.7	476.9
75.85		16.4	497.6
125.95		17.1	514.9
177.60		17.9	527.9

Table 2
Calculation conditions for numerical investigation.

	T_{in} (°C)	q (kW/m^3)	P (MPa)	G (kg/m^{3}s)	d (mm)	α (°)	buoyancy effects
case 1 (Weinberg, 1972)	14	56.7	7.58	564.32	19	0	strong
case 2 (Weinberg, 1972)	14	40.5	7.58	564.32	19	0 & 180	weak
case 3 (Weinberg, 1972)	20	50	7.58	437.3	19	0 & 180	strong
case 4 (Adebiyi and Hall, 1976)	15.4	15.1	7.59	384.4	22.14	90	weak
case 5 (Adebiyi and Hall, 1976)	21.1	21.4	7.607	201.6	22.14	90	strong
case a	15	50	7.58	550	19	0~180	weak
case b	15	20	7.58	550	19	0~180	strong

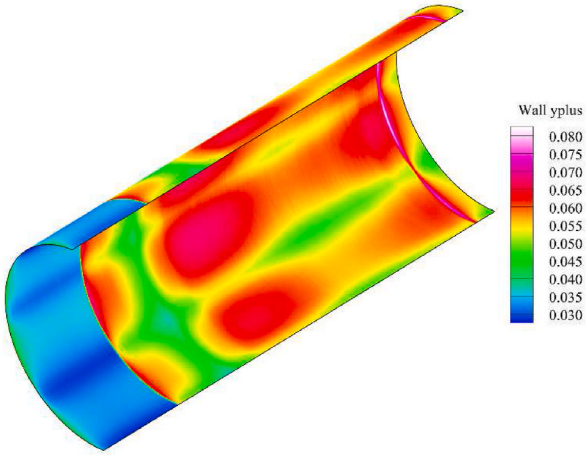

Fig. 3. Contours of wall y$^+$ with mesh settings for $n_1 = 13$, $n_2 = 11$, $n_3 = 70$.

mm, and a total length of 3000 mm. Adiabatic sections of 570 mm (30 d) and 151 mm (8 d) are placed at the inlet and outlet respectively to minimize the influence of inlet and outlet effects. The inclination angle and the circumferential angle of the tube are denoted by α and θ respectively.

To simulate the engineering scenario more realistically, a constant heat flux (equal to 0.854 times the heat flux of the inner wall q) is applied to the outer wall of the circular tube. The inlet and outlet boundary conditions are set as mass flow inlet and pressure outlet. The Coupled algorithm is chosen for pressure-velocity coupling. The temperature and pressure dependent properties of CO_2 used for the solver are obtained from NIST Standard Reference Database(Lemmon et al., 2002). Thermal properties of stainless steels are based on Sweet's work(Sweet et al., 1987), and the specific values are given in Table 1. The specific calculation conditions are shown in Table 2. Cases 1–5 are calculated for model validations; cases a and b are used for analyzing the flow structure and heat transfer of sCO_2 in tubes with different inclination angles.

3. Validation of numerical solution

3.1. Mesh independence verification

To improve the prediction accuracy of the near-wall area, the mesh is thinned along the wall. With reference to the research of Tang et al. (2016), the initial width is 0.0002 mm and the fixed growth rate is 1.06. As shown in Fig. 3, this setting can ensure that the dimensionless wall distance y$^+$ is always less than 0.1, ensuring the accuracy of the calculation results (it is generally believed that when $y^+ < 1$, the calculation has converged(Hou et al., 2022)). The axial mesh length is set to 2 mm, which has been extensively verified (Du et al., 2020; Guo et al., 2019; Tang et al., 2016). Sensitivity analysis was conducted on the remaining 3 edges of the mesh: circumferential edge n_1, radial edge of solid n_2 and radial edge of fluid n_2, as is shown in Fig. 4(a).

Nine sets of different grids of n_1, n_2 and n_3 were calculated, and the calculation results of wall temperature and central axis velocity under various mesh settings were shown in Fig. 5. As can be seen from Fig. 5(a and b), changes in n_1 and n_2 have basically no impact on the calculation results, while the calculation results of wall temperature only have a small difference, and the calculation results of velocity distribution are almost completely covered together. It can be seen from Fig. 5(c and d) that n_3 has a great impact on the calculation results, and the peak value of wall temperature will gradually decrease with the increase of n_3. When n_3 increases to 60, the calculation results remain basically unchanged. To obtain better convergence, the combination of $n_1 = 13$, $n_2 = 11$, $n_3 = 70$ was selected for the following calculation. The final meshing result is shown in Fig. 4(b).

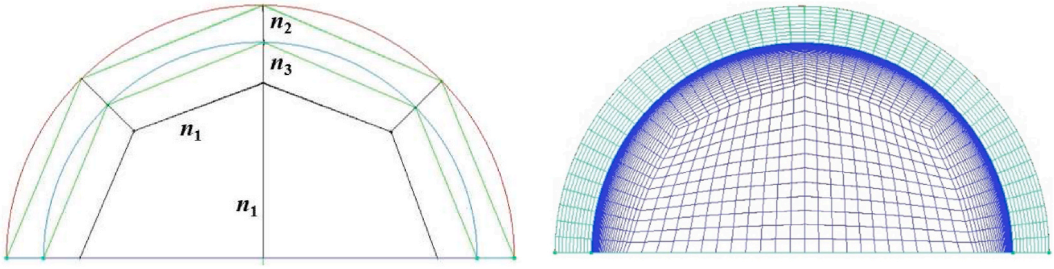

(a) Meshing method. (b) Mesh used in the simulation.

Fig. 4. Structured meshing division and its results.

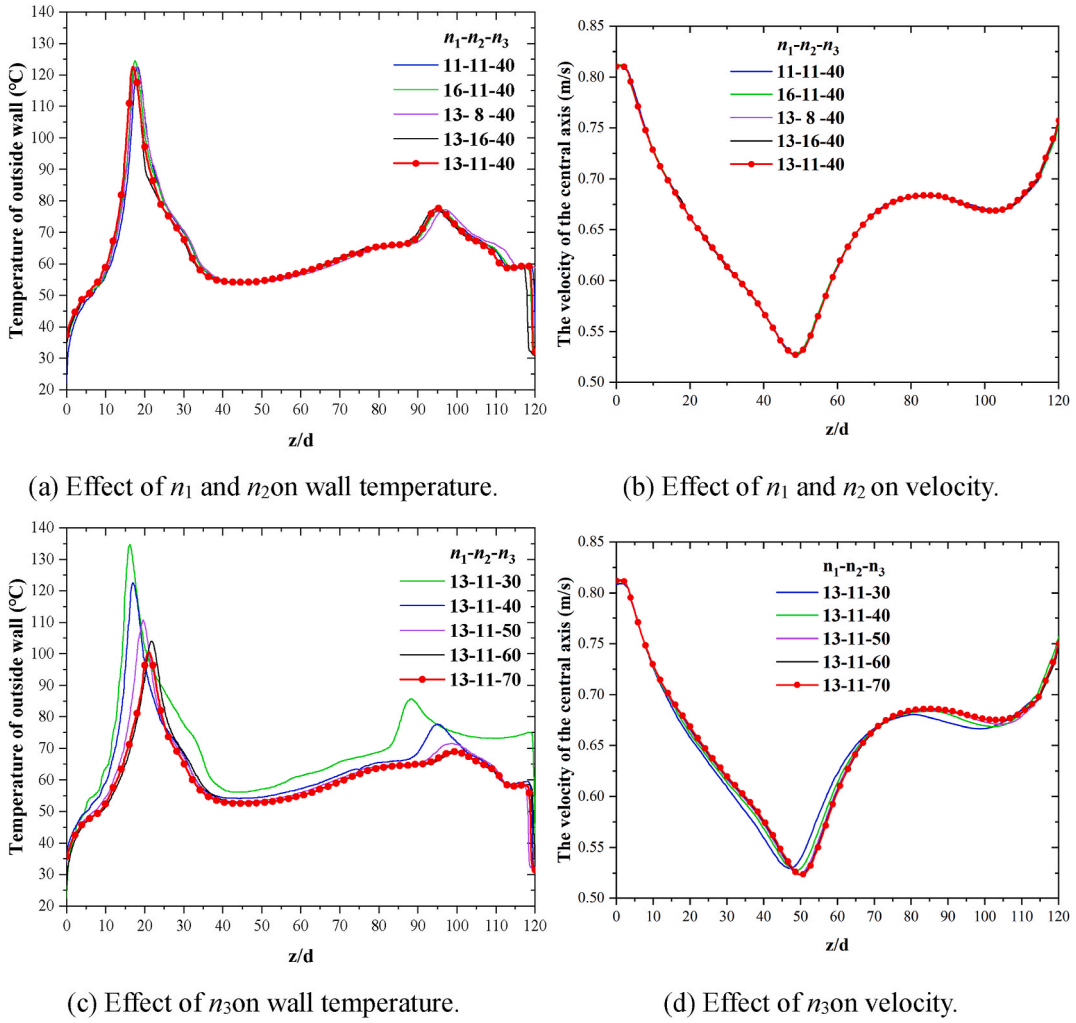

Fig. 5. Temperature and velocity distributions obtained from various grid calculations.

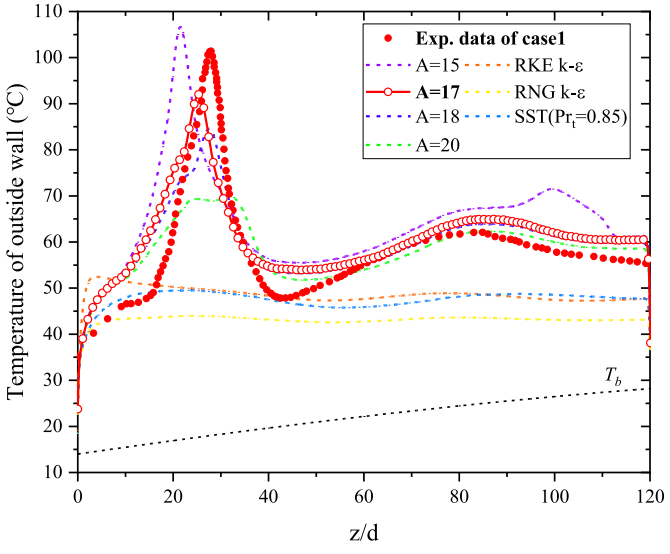

Fig. 6. The comparison between simulation and experimental results for case1.

3.2. Turbulence model correction and selection

Tang (Tang et al., 2016) proposed the TWL model after theoretical analysis and adopted a series of reasonable assumptions. There is an undetermined coefficient A in the TWL model. After selecting different values of A and comparing them with the experiment, Tang recommended the value of A to be 15, because $A = 15$ corresponds well with the experimental results. When Tang proposed this model, he used a 2D model that did not consider the solid domain, while the model adopted in our work was a 3D model that considered conjugate heat transfer. Therefore, it is necessary to conduct a comparative analysis again.

To ascertain the optimal value of parameter A, a sensitivity analysis was conducted by varying its values and subsequently comparing the simulation results against the experimental data obtained from case 1. The results of RNG $k-\epsilon$ and RKE $k-\epsilon$ turbulence models are also compared. As shown in Fig. 6, RNG $k-\epsilon$, RKE $k-\epsilon$ and SST $k-\omega$ ($Pr_t = 0.85$) turbulence models cannot calculate the peak value of wall temperature, while TWL model can simulate the peak value of wall temperature well. Moreover, the peak value of wall temperature calculated by TWL model decreases with the increase of A, and the peak position moves forward accordingly. Since the TWL model (A value of 17) predicted the wall temperature best compared to other turbulence models and different A-values, the TWL model was used for subsequent calculations. Tang et al. (2016) analyzed the difference of calculation results of different turbulence models in detail in his work, and the results showed that the TWL model could predict the peak wall temperature

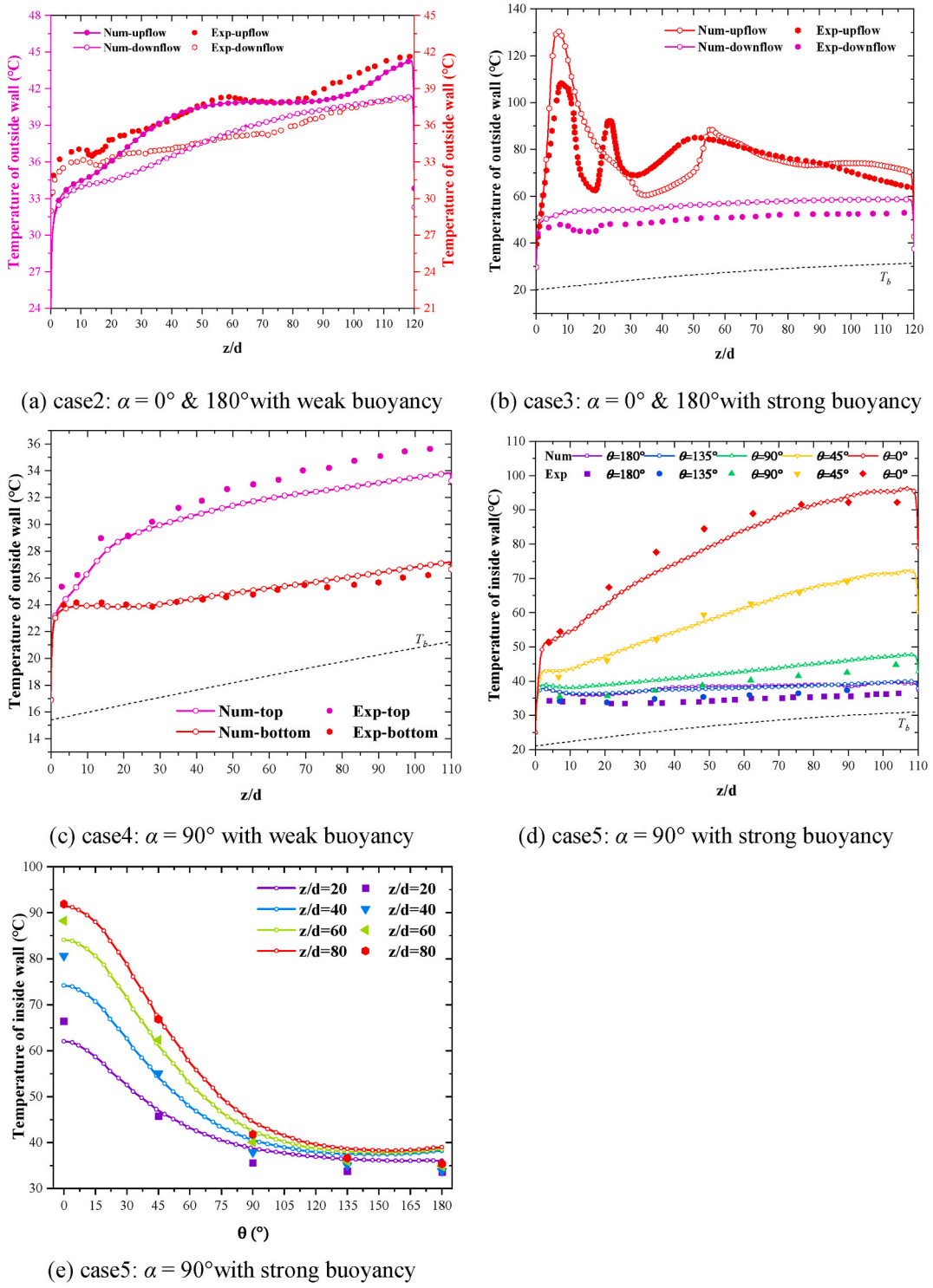

(a) case2: $\alpha = 0°$ & 180°with weak buoyancy

(b) case3: $\alpha = 0°$ & 180°with strong buoyancy

(c) case4: $\alpha = 90°$ with weak buoyancy

(d) case5: $\alpha = 90°$ with strong buoyancy

(e) case5: $\alpha = 90°$with strong buoyancy

Fig. 7. Extensive comparisons with experimental data.

because it could predict the restrain of turbulent mixing in the transition region, while other models cannot.

3.3. Model validation

To validate the numerical model, an extensive experimental comparison is performed. The vertical upward, vertical downward and horizontal flow under strong and weak buoyancy effects is validated. The verified experimental data used were measured by Weinberg (1972) and Adebiyi (Adebiyi and Hall, 1976), and detailed experimental conditions are shown in Table 2. Weinberg conducted an experimental study on convective heat transfer of sCO_2 in a vertical tube in 1972. The inner diameter d of the test section was 19 mm, the heating wall thickness was 1.625 mm, the total heating length was 129d, and there was a 64d adiabatic section at the entrance. Adebiyi and Hall conducted an experimental study on convective heat transfer of sCO_2 in a horizontal circular tube in 1976. The inner diameter d of the test section was 22.14 mm, the heating wall thickness was 1.63 mm, the total heating length was 110d, and there was a 55d adiabatic section at the entrance. In the experiment conducted by Adebiyi, thermocouples were affixed at

regular intervals of 76.2 mm along the tube, specifically at angular positions of 0°, 90°, 180°, and 270° from the top of the tube. Additionally, thermocouples were placed at intervals of 152.4 mm along the tube at angular positions of 45°, 135°, 225°, and 315°. In this section, a uniform body heat source heating method is used to be consistent with the experiments.

Fig. 7 shows the results of comparison between numerical simulation and experiment. The predicted temperature with the TWL model agrees well with the experimental data in all the cases. For the vertical flow under weak buoyancy effects, the calculated results match the experimental data closely, with only a temperature difference of less than 5 °C over most of the heating distance, as shown in Fig. 7(a). The TWL model successfully captures two wall temperature peaks in the upward flow under strong buoyancy effects (to the best of our knowledge, so far there is no turbulence model capable of simulating three peaks), as shown in Fig. 7(b). Fig. 7(c) shows the wall temperature comparison for the horizontal flow with weak buoyancy effects. The wall temperature at the bottom is remarkably consistent with the experimental results, though the wall temperature at the top is relatively low. Fig. 7(d and e) show the comparison of axial and circumferential wall temperatures for horizontal flow with strong buoyancy effects. The temperature distributions along the surfaces under strong buoyancy effects are still consistent, although the circumferential wall temperature difference can reach up to 50 °C, which will be explained in section 4.3.

4. Results and discussions

In order to assess the influence of the buoyancy in cases a and b, three criterions $\overline{Gr}/Re^{2.7}$(Jackson, 1979), Bo^*(Jackson et al., 1989) and Ri (Wang et al., 2018a, 2018b, 2019) were adopted, as defined below.

$$\frac{\overline{Gr}}{Re^{2.7}} > 10^{-5} \tag{8}$$

With:

$$\overline{Gr} = \frac{(\rho_b - \overline{\rho})\rho_b g d^3}{\mu_b^2} \tag{9}$$

$$\overline{\rho} = \frac{1}{T_w - T_b}\int_{T_b - T_w} \rho \mathrm{d}T \approx \begin{cases} \dfrac{(\rho_w + \rho_b)}{2}, & T_w < T_{pc} \text{ or } T_b > T_{pc} \\ \dfrac{\rho_b(T_{pc} - T_b) + \rho_w(T_w - T_{pc})}{T_w - T_b} & T_b < T_{pc} < T_w \end{cases} \tag{10}$$

$$Bo^* = \frac{Gr^*}{(Re^{3.425}Pr^{0.8})} > 5.7 \times 10^{-6} \tag{11}$$

With:

$$Gr^* = \frac{g\beta q d^4}{k_b v_b^2} \tag{12}$$

$$\beta = -\frac{1}{p}\left(\frac{\partial p}{\partial T}\right)_p \approx \frac{1}{\rho_b}\frac{\rho_w - \rho_b}{T_w - T_b} \tag{13}$$

$$Ri = \frac{Gr}{Re^2} \tag{14}$$

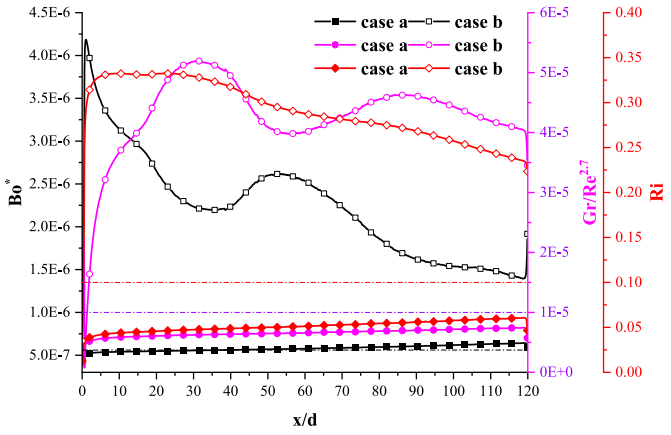

Fig. 8. Variations of buoyancy factor under case a and b with $\alpha = 0°$.

With:

$$Gr = \frac{\rho_b(\rho_w - \rho_b)g d^3}{\mu_b^2} \tag{15}$$

when $Ri < 0.1$, the buoyancy effect can be ignored; when $Ri > 10$, the buoyancy plays a major role; when $0.1 < Ri < 10$, at this time called mixed convection.

The dimensionless parameters for buoyancy effects of case a and b with $\alpha = 0°$ have been presented in Fig. 8. The dimensionless parameter $\overline{Gr}/Re^{2.7}$, Ri of case a is less than its threshold, and Bo^* is slightly greater than its threshold, which means buoyancy effects are weak in case a. However, all criterion of case b is greater than its threshold indicating that buoyancy effects play an important role in heat transfer and flow. Therefore, cases a and b are calculated to analyze how the flow and heat transfer gradually change as the inclination α increases from 0° to 180° under strong and weak buoyancy effects.

4.1. Flow structure with different inclination angles

The results and mechanisms of buoyancy effects on sCO_2 flow structure in detail from fundamental aspects are discussed in this section. Fig. 9(a–c) shows that when buoyancy effects are weak, the velocity peak location is in the upper part of the tube when $\alpha = 15°$, moves to the lower part when $\alpha = 60°$, and stays at the lower part when $\alpha = 90°$. However, Fig. 9(d–i) shows that when buoyancy effects are strong, the velocity peak is always at the upper part of the tube until $\alpha \leq 85°$. When $85° \leq \alpha \leq 90°$, the velocity peak quickly moves to the lower part of the tube from the upper part as α increases. Then the velocity peak position stays at the lower part of the tube until it returns to the center at $\alpha = 180°$. It can also be seen that when $\alpha = 0°$, the velocity near the wall is higher than that at the center, and the velocity distribution forms an 'M' shape due to the strong buoyancy effects.

Fig. 10 shows profiles of normalized velocity v/v_b along y-axis at $z/d = 110$, where v_b is determined by $v_b = G/\rho_b$. As α increases, the position of velocity peak will first move upward, then downward, and finally, return to the center. And the velocity peak position in the horizontal

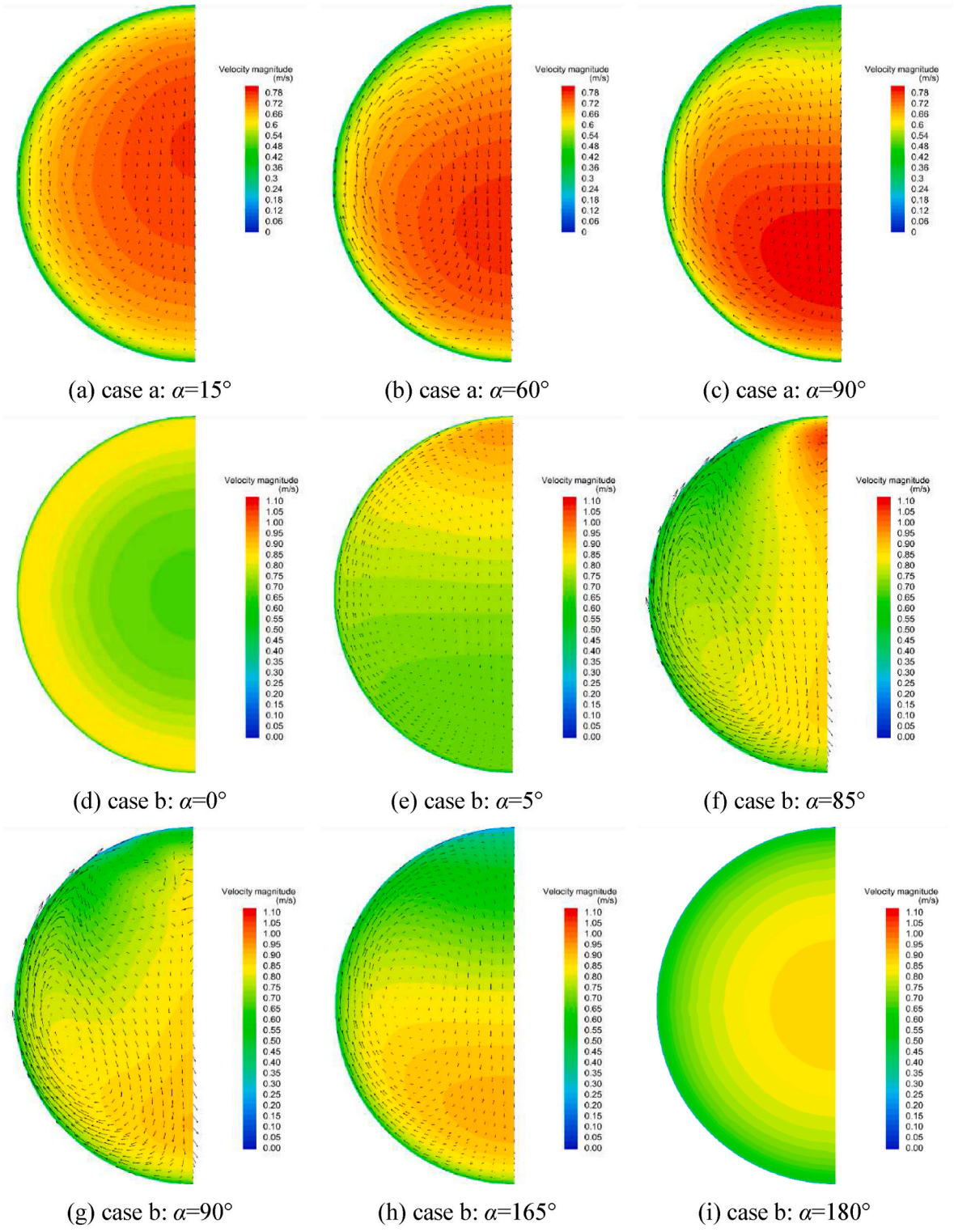

Fig. 9. Velocity magnitude contours and secondary flow velocity vectors at a $z/d = 110$.

tube is always in the lower part of the tube. The magnitude of the buoyancy primarily affects the threshold of α for the downward movement of the velocity peak. The velocity peak will move downward when $\alpha > 15°$ in case a with weak buoyancy effects, as displayed in Fig. 10(a). And the velocity peak position will move downward when $\alpha > 85°$ in case b with strong buoyancy effects, as displayed in Fig. 10(b).

The reasons for the above phenomenon are as follows. The buoyancy can be decomposed into two components: axial buoyancy and radial buoyancy. Axial buoyancy parallel to the sCO_2 mainstream increases the velocity magnitude of low-density fluid for upward flow and decreases it for downward flow. Radial buoyancy perpendicular to the mainstream induces a secondary flow, as shown in Fig. 9(c, g). Fig. 11 shows that the secondary flow transports the low-density sCO_2 to the upper part of the tube by upward flow and transfers the momentum to fluids in the lower part by downward flow through the core area mainstream. Therefore, the secondary flow tends to have the velocity peak position in the lower part of the tube.

When sCO_2 flows upward, axial buoyancy transports the low-density

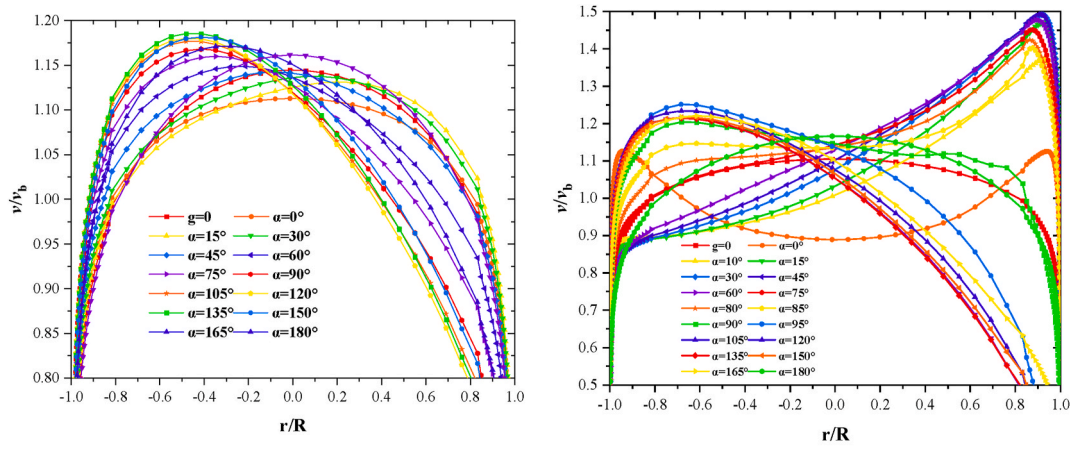

(a) case a (b) case b

Fig. 10. Profiles of normalized velocity v/v_b along y-axis at $z/d = 110$.

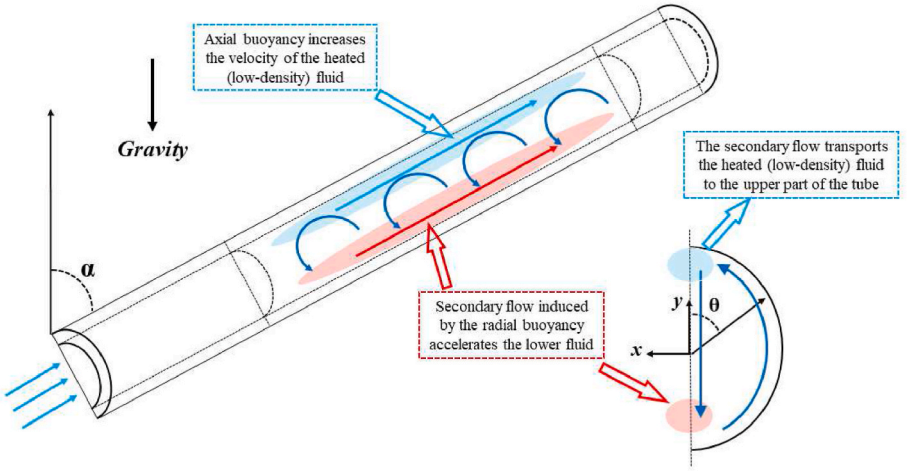

Fig. 11. The mechanism analysis diagram of buoyancy influencing flow structure for upward flow.

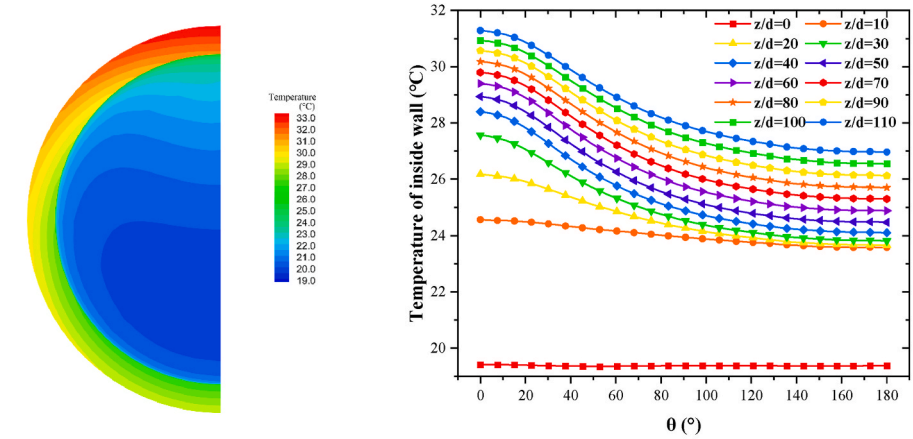

(a) Contour of temperature at z/d =110 (b) Variations of T_w and θ

Fig. 12. Schematic diagram of circumferential temperature distribution trend in case a of $\alpha = 90°$.

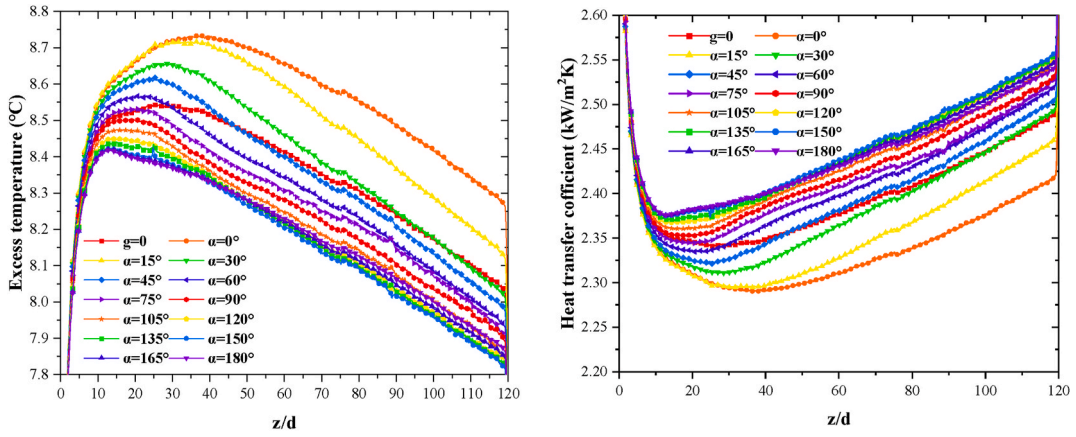

(a) Local excess temperature (T_w - T_b) (b) Heat transfer coefficient

Fig. 13. The variations of local excess temperature (T_w- T_b) and heat transfer coefficient of different α in case a.

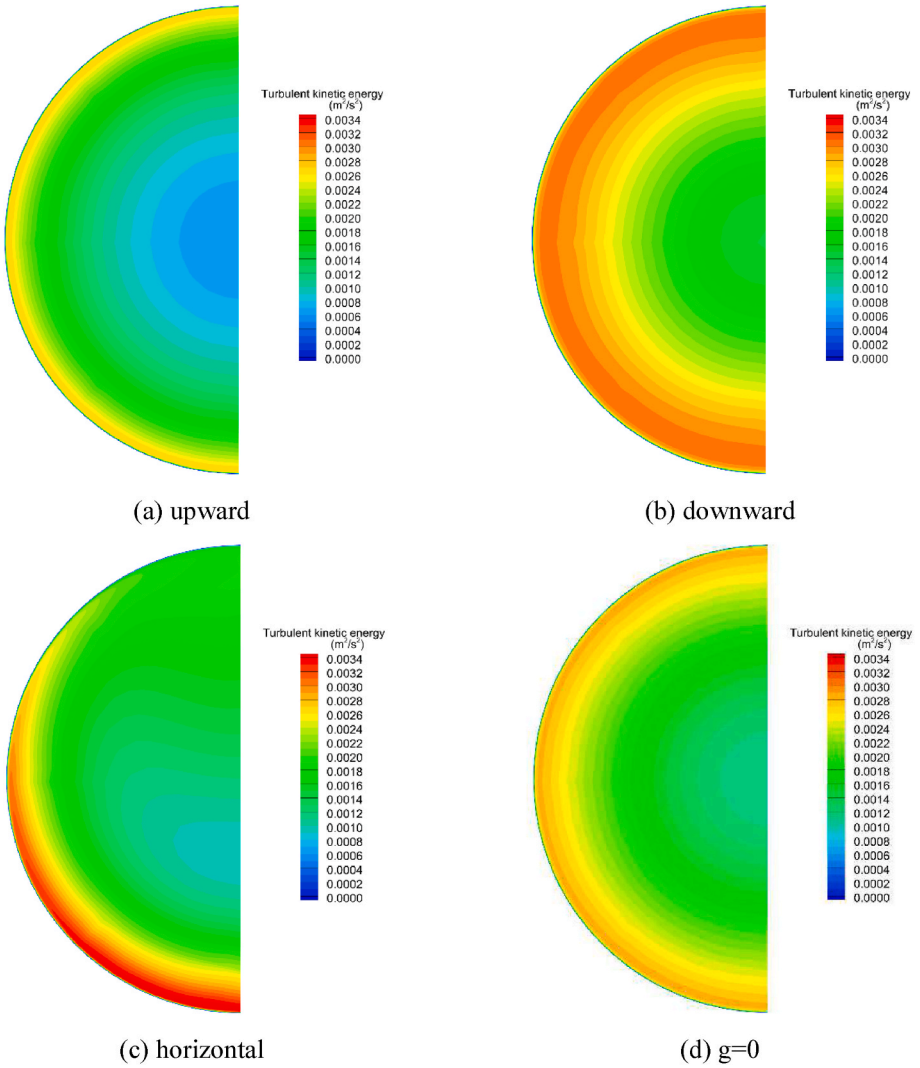

(a) upward (b) downward

(c) horizontal (d) g=0

Fig. 14. Contours of turbulent kinetic energy at $z/d = 110$ under different flow conditions.

fluid to the upper part of the tube, as shown in Fig. 11. This means that axial buoyancy tends to have the velocity peak in the upper part of the tube. Since axial and radial buoyancy have opposite effects, the position of the velocity peak moves upward and then downward as α increases for upward flow. The velocity peak position in the upper part of the tube indicates that axial buoyancy effects are stronger than radial buoyancy effects. When α is below the threshold for the downward movement of the velocity peak, axial buoyancy effects grow faster than radial

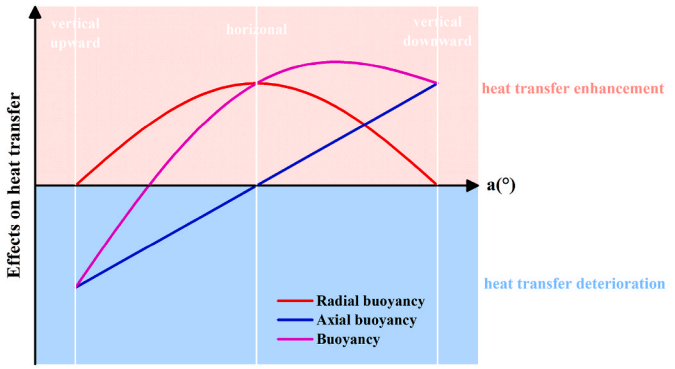

Fig. 15. Schematic diagram of the effects of buoyancy and its components on heat transfer.

buoyancy effects, and the velocity peak moves upward. Conversely, when α is above the threshold, the velocity peak moves downward. The threshold value increases with increasing buoyancy, which means that axial buoyancy effects increase more than radial buoyancy effects as buoyancy increases.

For horizontal flow, axial buoyancy disappears, so the velocity peak position is always in the lower part of the circular tube. For downward flow, axial buoyancy decreases the velocity of low-density fluid in the upper part, which also means that axial buoyancy tends to move the velocity peak position downward. Therefore, the velocity peak position is always in the lower part of the tube.

4.2. Heat transfer with weak buoyancy effects

This section will discuss the results and mechanisms of the influence of inclination angle on sCO_2 heat transfer under weak buoyancy effects. As shown in Fig. 12, when $\alpha = 90°$ (as well as other angles except 0° and 180°) the wall temperature will be uneven, with high temperature at the top and low temperature at the bottom. As mentioned in section 4.1, the secondary flow will transport the heated fluid to the upper part of the tube, and the velocity in the upper part is lower at most inclination angles resulting in a lower heat transfer coefficient at the upper part. According to Newton's law of cooling as Eq. (16), since the properties of sCO_2 do not change drastically with the $T_w < T_{pc}$ and the local heat flux is the same, the wall temperature at the top will be higher than that at the bottom.

$$T_w = T_f + \frac{q}{h(v, c_p, \mu, \cdots)} \tag{16}$$

Fig. 13 illustrates the trend of both the average excess temperature and heat transfer coefficient. The average excess temperature represents the disparity between the average inside wall temperature T_w and the bulk temperature T_b across the cross-sectional area. T_b is computed from the bulk enthalpy H_b calculated by Eq. (17). The heat transfer coefficient h is calculated from Eq. (18). Fig. 13(a) shows the excess temperature gradually decreases with the heating of sCO2, and accordingly, the heat transfer coefficient gradually increases, as displayed in Fig. 13(b). This is because T_b gradually approaches T_{pc} as sCO_2 is heated, and the specific heat increases as well, as shown in Fig. 1, which in turn enhances the heat transfer. The phenomenon has also been observed in Liu's experiments (Liu et al., 2014).

$$H_b = H_{in} + \frac{Power}{m}\frac{z}{l} = H_{in} + 4\frac{qz}{Gd} \tag{17}$$

$$h = \frac{q}{T_w - T_b} \tag{18}$$

Figs. 10(a) and Fig. 14(a, d) show that when the sCO_2 flows upward, the buoyancy force effects (although still weak) increase the velocity near the wall and decrease it in the central region, which causes a significant decrease in shear stress and turbulent kinetic energy (TKE). The reduction of TKE then reduces the turbulent diffusion of heat and further increases the wall temperature, as Fig. 13(a) shows. Similarly, Fig. 14(b, d) show that buoyancy effects increase the stress and TKE for vertical downflow, which enhances heat transfer. In the horizontal flow, the downward movement of the velocity peak increases the TKE at the bottom and enhances heat transfer, and decreases it at the top and weakens heat transfer. The enhancement in the lower part is greater than that in the upper part, so the overall heat transfer enhancement is shown. From the above analysis, it can be concluded that axial buoyancy effects weaken heat transfer in the upward flow and enhance it in the downward flow, and the secondary flow caused by radial buoyancy has a positive effect on sCO_2 heat transfer overall under weak buoyancy effects.

Fig. 15 shows the effects of buoyancy and its components on heat transfer as α varies. As α increases, axial buoyancy increases and radial buoyancy decreases, which leads to stronger heat transfer for upward flow. Axial buoyancy decreases and radial buoyancy increases, which results in stronger heat transfer for upward flow before $\alpha < 150°$ and weaker heat transfer after that in downward flow, as Fig. 13 shows. The above process also leads to an overall deterioration of heat transfer for $\alpha < 30°$, and an overall enhancement of heat transfer for $\alpha > 30°$.

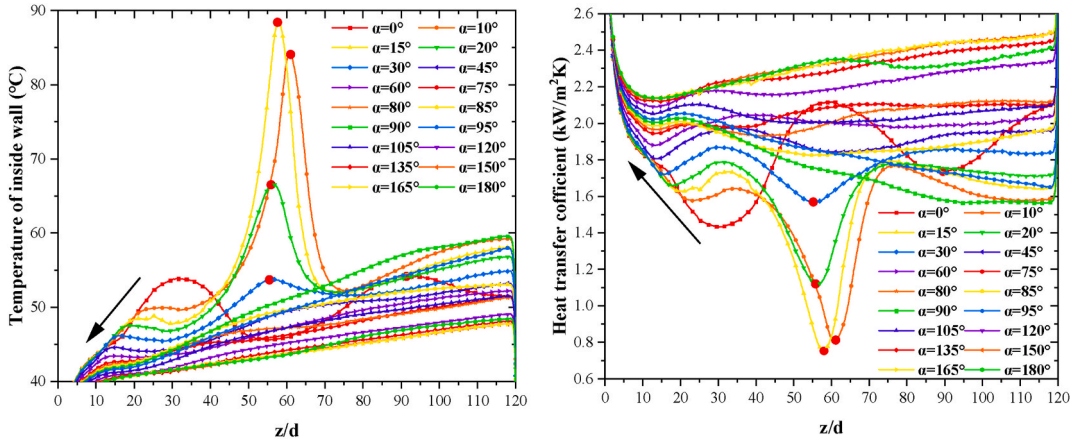

(a) Temperature of the inside wall (b) Heat transfer coefficient

Fig. 16. The variations of wall temperature and heat transfer coefficient of different α in case b.

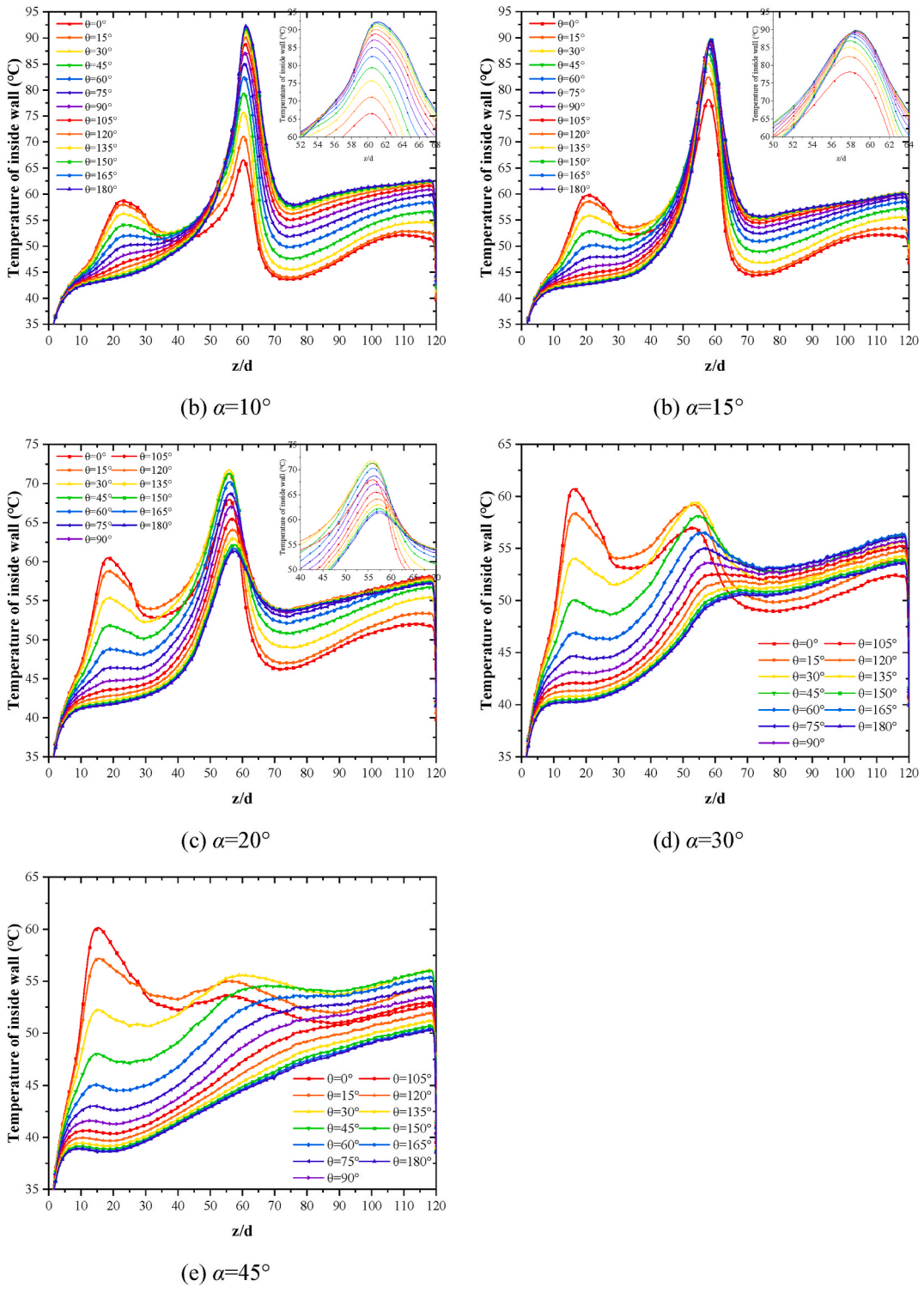

Fig. 17. The local wall temperature distribution with different inclination angle α in case b.

4.3. Heat transfer with strong buoyancy effects

Fig. 16 shows the trend of the inside wall temperature and heat transfer coefficient in case b under strong buoyancy effects. The figure shows that there are two wall temperature peaks under strong buoyancy effects. Cheng et al. (2017) analyzed the mechanisms of the two temperature peaks under vertical upward flow and found that buoyancy effects caused the first peak and shear stress caused the second peak. In this section, the phenomenon and mechanisms of the two wall temperature peaks changing with inclination angle are analyzed.

Fig. 17 shows a more detailed temperature distribution of the inside wall temperature with different inclination angles. It can be found that the first wall temperature peak is due to heat transfer deterioration at the top by comparing Fig. 17(a–e). Fig. 18 shows the profiles of velocity magnitude and turbulent kinetic energy along the y-axis with $\alpha = 20°$ and 30°. The secondary flow transports the heated fluid to the upper part of the tube and the wall heating makes the upper fluid reach T_{pc} quickly, which leads to a significant decrease in fluid density. Strong axial

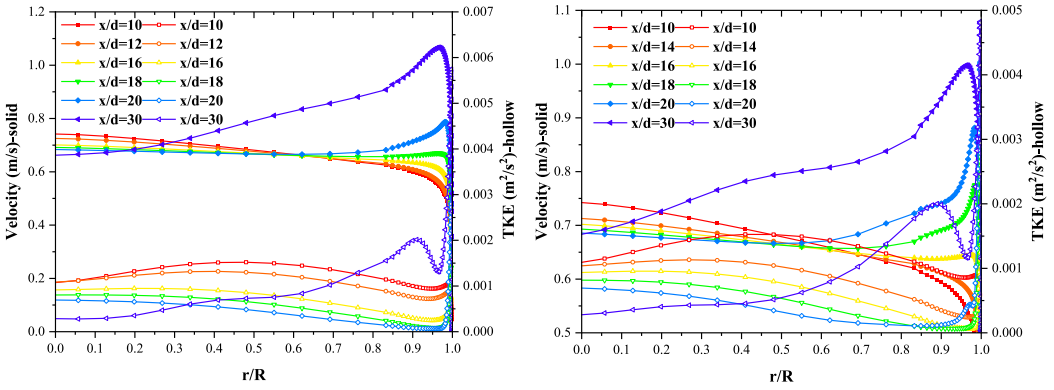

Fig. 18. Profiles of velocity and turbulent kinetic energy along *y*-axis with $\alpha = 20^{\circ}$ and 30°.

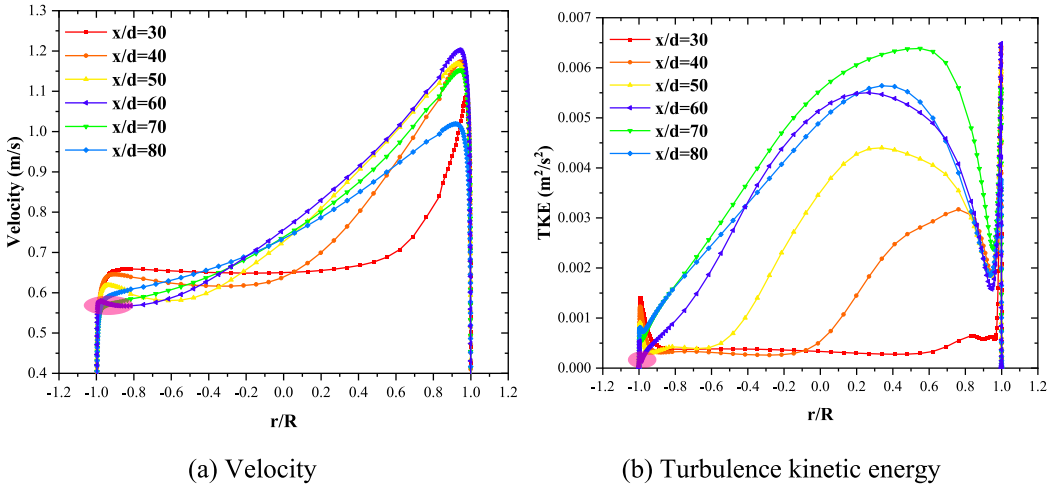

Fig. 19. Profiles of velocity and turbulent kinetic energy along *y* axis with $\alpha = 10^{\circ}$.

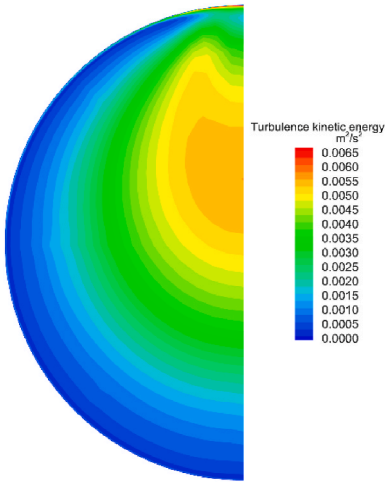

Fig. 20. Contours of turbulent kinetic energy at $z/d = 60$ in case b with $\alpha = 10^{\circ}$.

buoyancy effects increase the upper fluid velocity drastically. Fig. 17 shows that the velocity profile is nearly flat near the wall ($0.85 < r/R < 1$) when $z/d = 18$ for $\alpha = 20^{\circ}$ and $z/d = 16$ for $\alpha = 30^{\circ}$, resulting in a significant decrease of shear stress and TKE. The reduction of TKE then reduces the turbulent diffusion of heat and further increases the wall temperature. Because TKE drops almost to 0, heat transfer is mainly through conduction, so the wall temperature at the top ($\theta = 0^{\circ}$) is always around 60 °C when the first heat transfer deterioration occurs for $\alpha \leq 45^{\circ}$, as Fig. 17 shows. With continuous heating, the velocity magnitude increases continuously, TKE gradually recovers and heat transfer deterioration is mitigated for $z/d \geq 20$, as Fig. 18 shows. It can be concluded from Fig. 18 that axial buoyancy effects cause heat transfer deterioration at the top and then the first wall temperature peak. Fig. 17 also shows that the position where heat transfer deterioration occurs in advance gradually as α increases, peaking at $z/d = 25$ for $\alpha = 10^{\circ}$ and peaking at $z/d = 15$ for $\alpha = 45^{\circ}$. The reasons are as follows: the radial buoyancy is the result of the radial component of gravity $(g \bullet \sin(\alpha))$. Due to the existence of radial buoyancy, the low-density flow at the wall will flow upward, and the high-density fluid at the center of the pipe will move downward, thus inducing secondary flow. With the increase of α, the gravity radial component increases, the radial buoyancy effect is enhanced, and the secondary flow is enhanced, so that the heated sCO_2 is transported to the top faster, and the temperature of sCO_2 near the top reaches T_{pc} earlier.

The velocity magnitude near the top region increases continuously after the first temperature peak. Fig. 19 shows the profiles of velocity and turbulent kinetic energy along the y-axis for different z/d with $\alpha = 10^{\circ}$. In this phase, the shear stress caused by the velocity gradient

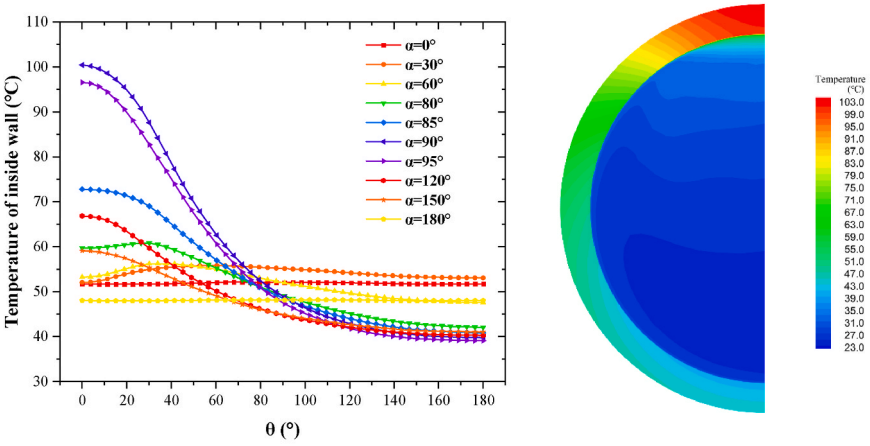

(b) Variations of T_w and θ at z/d=110 (a) Contour of temperature with α=90°

Fig. 21. Schematic diagram of circumferential temperature distribution trend in case b.

increases the velocity magnitude of the fluid in the lower part of the tube gradually. When the effect reaches the bottom at $z/d = 60$, the velocity near the lower part becomes flat, resulting in a significant decrease in TKE, as Fig. 19 shows. The decrease of TKE occurs near most of the walls except for the top, as Fig. 20 shows, which reduces the turbulent diffusion of heat and further increases the wall temperature, as Fig. 16 (a) shows. The above analysis shows that shear stress flattens the velocity profile near the wall except for the top, causing a decrease in TKE near the wall, which leads to the second wall temperature peak.

The heat transfer deterioration mechanism of the second peak changes with the increase of α compared to the vertical upward flow (the deterioration mechanism for vertical upward refers to Cheng's work (Cheng et al., 2017)) when the tube starts to incline ($\alpha < 15°$). The inclined tube has a greater velocity gradient, which causes greater shear stress and more severe heat transfer deterioration compared to vertical upward flow, as Fig. 16 shows. When α increases from 15° to 75, the secondary flow strength increases, the velocity of the lower fluid increases, the velocity gradient decreases, and the effect of shear stress decreases. Therefore, heat transfer deterioration is relieved as α increases ($\alpha > 15°$). This implies that a slight inclination of the circular tube causes more severe heat transfer deterioration for upward flow with strong buoyancy, which needs to be considered in engineering. Similar to the first peak, the position of the second wall temperature peak also shifts forward, because the secondary flow becomes stronger and accelerates the above process.

Fig. 21(b) shows the circumferential wall temperature distribution at $z/d = 110$ with different inclination angles. The circumferential wall temperature changes gradually from uniform to the highest temperature at $\theta = 30°$ as α increases, and when α increases to about 90°, the top wall temperature soars, turning into a distribution trend of higher temperature at the top and lower at the bottom, which is quite different from case a. The main reason for this phenomenon is that when $\alpha < 85°$, the velocity magnitude near the upper part is high, as Fig. 9 shows, resulting in an increase in TKE at this location, as Fig. 20 shows, which greatly enhances convection heat transfer. According to Newton's law of cooling in Eq. (16), although the fluid temperature is higher at the top, the high velocity magnitude increases HTC greatly, making the wall temperature at the top lower than a little further from the top ($\theta = 30°$). However, when α continues to increase to about 90°, the velocity peak moves to the lower part, and the thermophysical properties change to the gas-like phase because the fluid temperature is higher than T_{pc} (32.2 °C at 7.58 MPa). The change of flow field and thermophysical properties sharply reduces the local h at the top, resulting in a sharp rise in the top wall temperature. This is also the reason why sCO_2 heat transfer weakens again when α increases to near 90°, as Fig. 16 shows. This means that for horizontal flows with strong buoyancy, a slight inclination of the tube can mitigate heat transfer deterioration, which can be easily applied to engineering.

5. Conclusions

The study focused on the heat transfer and flow characteristics of supercritical pressure CO_2 within an inclined tube, particularly under weak ($G = 550$ kg/(m^2·s), $T_{in} = 15$ °C, $P_{out} = 7.58$ MPa, $q = 20$ kW/m^2) and strong ($G = 550$ kg/(m^2·s), $T_{in} = 15$ °C, $P_{out} = 7.58$ MPa, $q = 50$ kW/m^2) buoyancy effects using variable turbulent Prandtl number turbulence model. The phenomenon and mechanisms of the variation of flow and heat transfer with inclination angle were analyzed and discussed. From the obtained outcomes, the following conclusions can be summarized.

- The variable Pr_t model used could accurately predict heat transfer deterioration under the calculation conditions in this paper. An extensive experimental comparison was performed to validate the TWL model. The result shows that the predicted temperature with TWL model has the best agreement with all experiment data among selected RANS models. It is recommended that this model is used in designing the heat exchangers using the sCO_2 Brayton cycle.
- The buoyancy can be decomposed into two components: axial buoyancy and radial buoyancy. When sCO_2 flows upward, axial buoyancy moves the peak velocity position to the upper part of the tube, and when it flows downward, it moves it to the lower part. The secondary flow induced by radial buoyancy moves the velocity peak to the lower part of the tube. The combined effect of the two components makes the position of the peak velocity move upward, then downward, and finally back to the center as α increases.
- Under weak buoyancy effects, axial buoyancy effects weaken heat transfer in the upward flow and enhance it in the downward flow, and the secondary flow caused by radial buoyancy has a positive effect on sCO_2 heat transfer overall. Therefore, sCO_2 heat transfer is gradually enhanced before $\alpha < 150°$ and weakened after that with the increase of α.
- Under strong buoyancy effects, there are two wall temperature peaks in inclined tubes. The buoyancy effect causes the first peak, which flattens the velocity distribution near the top and reduces TKE and heat transfer. The shear stress causes the second peak, which flattens the velocity profile near the wall except for the top, reducing TKE and heat transfer again.
- A notable finding is that the best heat transfer occurs at $\alpha = 150°$ for both strong and weak buoyancy effects, a slight inclination of the

tube causes more severe heat transfer deterioration for upward flow under strong buoyancy effects, and a slight inclination of the tube mitigates heat transfer deterioration for horizontal flows under strong buoyancy.

Funding

This work was supported by the National Natural Science Foundation of China [Grant numbers U22241278].

CRediT authorship contribution statement

Junren Hou: Investigation, Methodology, Software, Validation, Writing - original draft. **Yuan Zhou:** Resources, Supervision, Writing - review & editing. **Yuan Yuan:** Methodology, Writing - original draft. **Shanfang Huang:** Supervision, Writing - original draft.

Declaration of competing interest

The authors declare that they have no known competing financial interests or personal relationships that could have appeared to influence the work reported in this paper.

Data availability

Data will be made available on request.

References

Abe, K., Kondoh, T., Nagano, Y., 1994. A new turbulence model for predicting fluid flow and heat transfer in separating and reattaching flows—I. Flow field calculations. Int. J. Heat Mass Tran. 37, 139–151.
Adebiyi, G.A., Hall, W., 1976. Experimental investigation of heat transfer to supercritical pressure carbon dioxide in a horizontal pipe. Int. J. Heat Mass Tran. 19, 715–720.
Ahn, Y., Bae, S.J., Kim, M., Cho, S.K., Baik, S., Lee, J.I., Cha, J.E., 2015. Review of supercritical Co2 power cycle technology and current status of research and development. Nucl. Eng. Technol. 47, 647–661.
Bae, Y.-Y., Kim, H.-Y., Kang, D.-J., 2010. Forced and mixed convection heat transfer to supercritical CO2 vertically flowing in a uniformly-heated circular tube. Exp. Therm. Fluid Sci. 34, 1295–1308.
Buzzi, F., Pucciarelli, A., Ambrosini, W., 2019. On the mechanism of final heat transfer restoration at the transition to gas-like fluid at supercritical pressure: a description by CFD analyses. Nucl. Eng. Des. 355.
Chen, J., Zhang, D., Song, P., Wang, X., Wang, S., Liang, Y., Qiu, S., Zhang, Y., Wang, M., Su, G., 2018. CFD investigation on thermal-hydraulic behaviors of a wire-wrapped fuel subassembly for sodium-cooled fast reactor. Ann. Nucl. Energy 113, 256–269.
Cheng, H., Zhao, J., Rowinski, M.K., 2017. Study on two wall temperature peaks of supercritical fluid mixed convective heat transfer in circular tubes. Int. J. Heat Mass Tran. 113, 257–267.
Diao, L., Chen, Y., Li, Y., 2019. Nonuniform heat transfer of supercritical pressure carbon dioxide under turbulent cooling condition in circular tubes at various inclination angles. Nucl. Eng. Des. 352.
Dong, W., Wei, W., Zhao, L., Gang, X., Zhou, T., Ba, J., 2022. Numerical study on flow and heat transfer of S−CO2 in inclined tubes under different flow conditions. Case Stud. Therm. Eng. 35.
Dostal, V., Driscoll, M.J., Hejzlar, P., 2004. A Supercritical Carbon Dioxide Cycle for Next Generation Nuclear Reactors.
Du, X., Lv, Z., Yu, X., Cao, M., Zhou, J., Ren, Y., Qiu, Q., Zhu, X., 2020. Heat transfer of supercritical CO2 in vertical round tube: a considerate turbulent Prandtl number modification. Energy 192.
Fluent, A., 2011. Ansys Fluent Theory Guide, vol. 15317. Ansys Inc., USA, pp. 724–746.
Forooghi, P., Hooman, K., 2013. Numerical study of turbulent convection in inclined pipes with significant buoyancy influence. Int. J. Heat Mass Tran. 61, 310–322.
Guo, J., Xiang, M., Zhang, H., Huai, X., Cheng, K., Cui, X., 2019. Thermal-hydraulic characteristics of supercritical pressure CO2 in vertical tubes under cooling and heating conditions. Energy 170, 1067–1081.
He, S., Wang, M., Zhang, J., Tian, W., Qiu, S., Su, G., 2021. Numerical simulation of three-dimensional flow and heat transfer characteristics of liquid lead–bismuth. Nucl. Eng. Technol. 53, 1834–1845.
Hou, J.R., Song, Q.K., Leng, H.J., Xue, C.H., Yuan, Y., Zhou, Y., 2022. A non-destructive model for thermal-hydraulics of wire-wrapped rod bundle and wire-rod contact corner microscopic behavior. Prog. Nucl. Energy 154.
Jackson, J., 1979. Influences of buoyancy on heat transfer to fluids flowing in vertical tubes under turbulent conditions. Turbulent forced convection in channels and bundles 2, 613–640.
Jackson, J., Cotton, M., Axcell, B., 1989. Studies of mixed convection in vertical tubes. Int. J. Heat Fluid Flow 10, 2–15.
Kim, D.E., Kim, M.-H., 2011. Experimental investigation of heat transfer in vertical upward and downward supercritical CO2 flow in a circular tube. Int. J. Heat Fluid Flow 32, 176–191.
Lemmon, E.W., Huber, M.L., McLinden, M.O., 2002. NIST reference fluid thermodynamic and transport properties–REFPROP. NIST standard reference database 23, v7.
Li, J., Fang, D., Guo, C., Wang, M., Deng, J., Tian, W., Qiu, S., Su, G., 2020. Numerical study on the thermal hydraulic characteristics in a wire-wrapped assembly of LFRs. Front. Energy Res. 8, 548065.
Liu, Z.-B., He, Y.-L., Yang, Y.-F., Fei, J.-Y., 2014. Experimental study on heat transfer and pressure drop of supercritical CO2 cooled in a large tube. Appl. Therm. Eng. 70, 307–315.
Qin, H., Wang, C., Wang, M., Zhang, D., Tian, W., Su, G., Qiu, S., 2019. Numerical investigation on thermal-hydraulic characteristics of NaK in a helical wire wrapped annulus. Int. J. Heat Mass Tran. 145, 118689.
Sánchez, D., Muñoz de Escalona, J.M., Chacartegui, R., Muñoz, A., Sánchez, T., 2011. A comparison between molten carbonate fuel cells based hybrid systems using air and supercritical carbon dioxide Brayton cycles with state of the art technology. J. Power Sources 196, 4347–4354.
Singh, M.P., Singh, S., 2019. Non-linear stability analysis of supercritical carbon dioxide flow in inclined heated channel. Prog. Nucl. Energy 117.
Sun, H., Pellegrini, M., Wang, C., Suzuki, S., Okamoto, K., Tian, W., Qiu, S., Su, G., 2022. CFD simulation based on film model of high temperature potassium heat pipe at different positions: horizontal, vertical, and 45° inclined. Prog. Nucl. Energy 154, 104442.
Sweet, J., Roth, E., Moss, M., 1987. Thermal conductivity of Inconel 718 and 304 stainless steel. Int. J. Thermophys. 8, 593–606.
Tang, G., Shi, H., Wu, Y., Lu, J., Li, Z., Liu, Q., Zhang, H., 2016. A variable turbulent Prandtl number model for simulating supercritical pressure CO2 heat transfer. Int. J. Heat Mass Tran. 102, 1082–1092.
Wang, C., Li, P., Zhang, D., Tian, W., Qiu, S., Su, G., Deng, J., 2022. Experimental study on the influence of heating surface inclination angle on heat transfer and CHF performance for pool boiling. Nucl. Eng. Technol. 54, 61–71.
Wang, J., Guan, Z., Gurgenci, H., Hooman, K., Veeraragavan, A., Kang, X., 2018a. Computational investigations of heat transfer to supercritical CO2 in a large horizontal tube. Energy Convers. Manag. 157, 536–548.
Wang, J., Guan, Z., Gurgenci, H., Veeraragavan, A., Kang, X., Sun, Y., Hooman, K., 2018b. Numerical study on cooling heat transfer of turbulent supercritical CO2 in large horizontal tubes. Int. J. Heat Mass Tran. 126, 1002–1019.
Wang, J., Li, J., Gurgenci, H., Veeraragavan, A., Kang, X., Hooman, K., 2019. Computational investigations on convective flow and heat transfer of turbulent supercritical CO2 cooled in large inclined tubes. Appl. Therm. Eng. 159.
Wang, K., He, Y.-L., 2017. Thermodynamic analysis and optimization of a molten salt solar power tower integrated with a recompression supercritical CO 2 Brayton cycle based on integrated modeling. Energy Convers. Manag. 135, 336–350.
Weinberg, R.S., 1972. Experimental and Theoretical Study of Buoyancy Effects in Forced Convection to Supercritical Pressure Carbon Dioxide. University of Manchester.
Wu, P., Ma, Y.D., Gao, C.T., Liu, W.H., Shan, J.Q., Huang, Y.P., Wang, J.F., Zhang, D., Ran, X., 2020. A review of research and development of supercritical carbon dioxide Brayton cycle technology in nuclear engineering applications. Nucl. Eng. Des. 368.
Yang, C., Xu, J., Wang, X., Zhang, W., 2013. Mixed convective flow and heat transfer of supercritical CO2 in circular tubes at various inclination angles. Int. J. Heat Mass Tran. 64, 212–223.
Yang, X., Su, G., Tian, W., Wang, J., Qiu, S., 2010. Numerical study on flow and heat transfer characteristics in the rod bundle channels under super critical pressure condition. Ann. Nucl. Energy 37, 1723–1734.
Yu, G., Jiang, C., Wang, L., Su, G., Qiu, S., 2018. A new method on fluid-to-fluid scaling for heat transfer in tubes at supercritical pressures. Int. J. Heat Mass Tran. 126, 809–822.
Zhang, H., Guo, J., Huai, X., Cui, X., Cheng, K., 2019. Buoyancy effects on coupled heat transfer of supercritical pressure CO2 in horizontal semicircular channels. Int. J. Heat Mass Tran. 134, 437–449.